Science Bulletin 68 (2023) 165–172

Contents lists available at ScienceDirect

Science Bulletin

journal homepage: www.elsevier.com/locate/scib

Article

Charge instability of topological Fermi arcs in chiral crystal CoSi

Zhicheng Rao [a,b,c,1], Quanxin Hu [a,c,1], Shangjie Tian [d,e,1], Qing Qu [b,1], Congrun Chen [b], Shunye Gao [a,c], Zhenyu Yuan [a,c], Cenyao Tang [a,c], Wenhui Fan [a,c], Jierui Huang [a,c], Yaobo Huang [f], Li Wang [g], Lu Zhang [a,c], Fangsen Li [g], Kedong Wang [b], Huaixin Yang [a,c,h], Hongming Weng [a,c,h], Tian Qian [a,c,h], Jinpeng Xu [a,c,i,*], Kun Jiang [a,c], Hechang Lei [e,*], Yu-Jie Sun [b,a,*], Hong Ding [a,h,i,2]

[a] Beijing National Laboratory for Condensed Matter Physics and Institute of Physics, Chinese Academy of Sciences, Beijing 100190, China
[b] Department of Physics, Southern University of Science and Technology, Shenzhen 518055, China
[c] School of Physical Sciences, University of Chinese Academy of Sciences, Beijing 100049, China
[d] School of Materials Science and Engineering, Anhui University, Hefei 230601, China
[e] Laboratory for Neutron Scattering, and Beijing Key Laboratory of Optoelectronic Functional Materials MicroNano Devices, Department of Physics, Renmin University of China, Beijing 100872, China
[f] Shanghai Synchrotron Radiation Facility, Shanghai Advanced Research Institute, Chinese Academy of Sciences, Shanghai 201204, China
[g] Vacuum Interconnected Nanotech Workstation (Nano-X), Suzhou Institute of Nano-Tech and Nano-Bionics (SINANO), Chinese Academy of Sciences, Suzhou 215123, China
[h] Songshan Lake Materials Laboratory, Dongguan 523808, China
[i] CAS Center for Excellence in Topological Quantum Computation, University of Chinese Academy of Sciences, Beijing 100190, China

ARTICLE INFO

Article history:
Received 23 August 2022
Received in revised form 9 December 2022
Accepted 31 December 2022
Available online 5 January 2023

Keywords:
Topological boundary states
Fermi arcs
Charge density wave
Many-body effect
Chiral crystal

ABSTRACT

Topological boundary states emerged at the spatial boundary between topological non-trivial and trivial phases, are usually gapless, or commonly referred as metallic states. For example, the surface state of a topological insulator is a gapless Dirac state. These metallic topological boundary states are typically well described by non-interacting fermions. However, the behavior of topological boundary states with significant electron–electron interactions, which could turn the gapless boundary states into gapped ordered states, e.g., density wave states or superconducting states, is of great interest theoretically, but is still lacking evidence experimentally. Here, we report the observation of incommensurable charge density wave (CDW) formed on the topological boundary states driven by the electron–electron interactions on the (001) surface of CoSi. The wavevector of CDW varies as the temperature changes, which coincides with the evolution of topological surface Fermi arcs with temperature. The orientation of the CDW phase is determined by the chirality of the Fermi arcs, which indicates a direct association between CDW and Fermi arcs. Our finding will stimulate the search of more interactions-driven ordered states, such as superconductivity and magnetism, on the boundaries of topological materials.

1. Introduction

The discovery of topological materials revolutionized our view on phase classification in condensed matter physics [1–5]. A common characteristic of topological materials, like topological insulators and semimetals, is the presence of nontrivial gapless boundary states, which are normally robust against symmetry-allowed perturbations owing to topological protection of the bulk. The topological boundary states not only directly reflect their topological properties, but also result in many exotic physical phenomena, such as quantum Hall conductivity [6,7], chiral magnetic effect [8] and anomalous quantum oscillations [9,10]. Typically, the physics of topological boundary states of topological materials are well captured from the perspective of non-interacting fermions. For example, density functional calculations have scored tremendous successes in predicting topological electronic materials and their boundary states [11–13]. On the other hand, electron–electron interactions also give rise to many fascinating phenomena, including unconventional superconductivity [14,15], Mott transition [16] and charge density wave (CDW) [17,18]. Therefore, the destiny of topological boundary states under electron–electron interactions emerges as an interesting question.

* Corresponding authors.
E-mail addresses: xujp@iphy.ac.cn (J. Xu), hlei@ruc.edu.cn (H. Lei), sunyj@sustech.edu.cn (Y.-J. Sun).
[1] These authors contributed equally to this work.
[2] Current affiliation: Tsung-Dao Lee Institute & School of Physics and Astronomy, Shanghai Jiao Tong University, Shanghai 200240, China.

https://doi.org/10.1016/j.scib.2023.01.001
2095-9273/

In Dirac and triply-degenerate semimetals, the "Fermi arcs" formed by topological boundary states are not topologically protected since the Chern number is zero for Dirac nodes and undefined for three-degenerate nodes [19–22]. Though the topological boundary states form robust Fermi arcs in Weyl semimetals, such as TaAs-family [23,24], (Mo,W)Te_2 [25,26] and $Co_3Sn_2S_2$ [27], all these Weyl semimetals are not good candidates for studying the many-body effect of topological boundary states because of narrow nontrivial energy windows, short Fermi arcs, and other trivial states coexisting. Drumhead-like boundary states in topological nodal-line semimetals have been proposed as ideal candidates for the many-body effect in theory due to the nearly flat surface band with large density of states in the vicinity of Fermi energy (E_F) [28]. However, clear experimental evidence is still elusive.

Recently, transition metal silicides (CoSi-family) with nonsymmorphic space group $P2_13$, dubbed as chiral crystals, have attracted wide attentions [29–35]. The topological nodes of bulk states at the Brillouin zone (BZ) center Γ and corner R points carry opposite Chern numbers near E_F [31–34]. On the surface of chiral crystals, the Fermi surface (FS) just consists of two Fermi arcs traversing the whole surface BZ, as shown in angle-resolved photoemission spectroscopy (ARPES) intensity map at the Fermi level (E_F) (Fig. 1b). The extremely long Fermi arcs and the simplicity of the chiral crystals provide an ideal platform to explore the many-body effect induced by the topological boundary states.

In this work, we report the observation of an incommensurable CDW on the (001) surface of CoSi while this CDW is missing on the bulk and other surfaces. This incommensurate CDW is directly related to the instability of CoSi long Fermi arc and correlation, which provides a standard example of correlated topological boundary states.

2. Materials and methods

2.1. Materials

Single crystals of CoSi were grown by the chemical vapor transport method. Co and Si powders in 1:1 molar ratio were put into a silica tube with a length of 200 mm and an inner diameter of 14 mm. Then, 200 mg I_2 was added into the tube as a transport reagent. The tube was evacuated down to 10^{-2} Pa and sealed under the vacuum. The tubes were placed in a two-zone horizontal tube furnace. The source and growth zones were raised to 950 and 800 K in 2 days, and were then held there for 7 days. Shiny crystals with lateral dimensions up to several millimeters can be obtained.

2.2. Surface preparation of CoSi

The structure of CoSi single crystal is simple cubic. It is difficult to obtain a flat surface by mechanical cleaving owing to the strong covalent bond and lack of a preferred cleaving plane. So, we used the *in-situ* sputtering and annealing method to obtain an atomically flat plane on the (001) and (111) surfaces [36]. Firstly, we verified the (001) and (111) surfaces of CoSi by Laue and X-ray diffraction (XRD) and subsequently mechanically polished them to a mirror finish on the surface. The atomically flat surface was prepared by Ar ion sputtering for 1 h and annealing at 760 °C for 30 min repeatedly in an ultra-high vacuum with a base pressure of 1×10^{-9} torr. Reflection high-energy electron diffraction (RHEED) was carried out to monitor the quality of the sample surface.

2.3. Scanning tunneling microscope (STM) and ARPES measurements

STM experiments were carried out in a low temperature ultra-high vacuum STM system, Unisoku USM-1300. Topographic images were acquired in the constant-current mode with a tungsten tip. Before the measurements, STM tips were heated by e-beam and calibrated on a clean Ag surface. The scanning settings of all the topographies were under 500 mV of bias voltages and 100 pA of setpoints unless specifically mentioned. Differential conductance spectra were acquired by a standard lock-in technique at a reference frequency of 973 Hz unless specifically mentioned. ARPES measurements were performed at the "Dreamline" beamline of the Shanghai Synchrotron Radiation Facility (SSRF) with a Scienta Omicron DA30L analyzer. The Fermi level is calibrated by measuring a clean gold sample at corresponding temperatures. All measurements were *in-situ* performed. The kinetic energy of low energy electron diffraction (LEED) patterns is 218 keV.

2.4. Transmission electron microscopy measurements

The microscopic characterizations of CoSi were performed with a JEOL-2100F electron microscope operated at a voltage of 200 kV. The specimen was prepared by crashing the crystals in acetone and deposited on a carbon film suspended on a copper grid. *In-situ* low-temperature TEM experiments were performed using a liquid-nitrogen-cooled specimen holder. High quality of CoSi crystals was confirmed by high resolution transmission electron microscope (HRTEM).

3. Results and discussion

We carried out scanning tunneling microscopy/spectroscopy (STM/S) experiments on the atomically flat CoSi surfaces prepared by *in-situ* repeated sputtering and annealing (see Section 2.2 Materials and methods for details). Fig. 1e presents an STM topographic image obtained on the (001) surface at 4.2 K. The square lattice with a period of ~4.43 Å (the lattice constant is 4.44 Å) shows that the structure of the (001) surface is stable after the sputtering-annealing process. In addition, a stripe-like superlattice modulation is also discernible. We extracted the period λ and angle α of the superlattice modulation by fast Fourier transformation (FFT), as shown in Fig. 1g. The value of λ is about $8.16a_0$ and the angle α between the superlattice and the [100] direction is about 34.2°, which indicates that the stripe-like superlattice modulation has an incommensurable period.

We then performed scanning tunneling spectroscopy (STS) measurements on the stripe superlattice region (Fig. 1c), and found that the differential conductance spectrum exhibits an energy gap-like feature extending from −22 to +20 meV around E_F. On the contrary, on the defect-rich surface, the density of states is gapless near E_F (Fig. S6c online). It suggests that the energy gap near E_F is induced by the superlattice. Furtherly, it is noted that the superlattice seems to only appear on high-quality surfaces, while it is absent on defect-rich surfaces (Fig. S6c online). On their corresponding surface, the ARPES intensity plot also shows that the Fermi arcs are disconnected around time reversal invariant point $\bar{X}$ on high-quality surface (Fig. 1b) while they are continuous in defect-rich samples (Fig. S6f online).

We also performed STM measurements on the (111) surface of CoSi, on which the Fermi arcs are absent because the Γ and R points are projected onto the same point on surface BZ. Fig. 1f and h show the atomically resolved hexagon lattice while the stripe superlattice modulation disappears on the surface. The fact that the stripe superlattice only exists on a specific surface implies that its origin is not from the bulk states. In addition, we carried out high-resolution transmission electron microscope (TEM) measurements on the (001) surface of CoSi (Fig. 1d). The absence of the satellite spots corresponding to the stripe-like superlattice in the

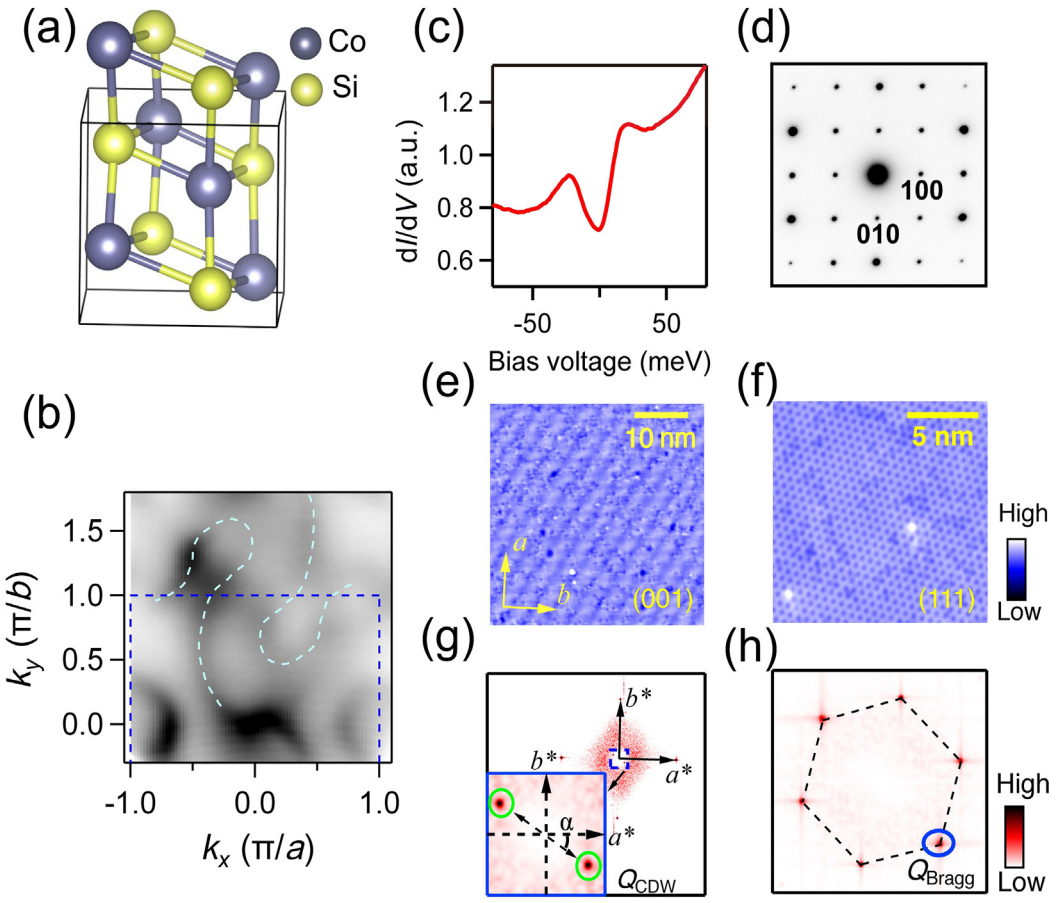

Fig. 1. (Color online) Stripe-like superlattice modulation on (001) surface of CoSi. (a) Crystal structure of CoSi. (b) ARPES intensity map at E_F, measured with $h\nu$ = 55 eV. The dashed lines indicate the Fermi arcs. (c) Tunneling differential conductance spectrum. An energy gap-like feature extends from −20 to +22 meV around E_F. (d) Typical selected area electron diffraction pattern taken along the [001] zone axis at 100 K, showing the stripe-like modulation absent in the bulk of CoSi. (e) Atomically resolved STM topographic image (40 nm × 40 nm) of the CoSi (001) surface taken at 4.2 K, showing the stripe-like superlattice. (f) STM topographic of the CoSi (111) surface taken at 4.2 K, showing a hexagonal lattice structure. (g) Fourier transform of the (001) surface topographic image of CoSi. The zoom-in image (insert) marked by the blue box shows the spots (green circle) corresponding to the stripe-like superlattice modulation. (h) Fourier transform of the (111) surface topographic image, showing no superlattice on the (111) surface.

selected area electron diffraction (SAED) pattern also confirms that it is absent in the bulk of CoSi. Therefore, we conclude that the stripe-like superlattice originates from the (001) surface of CoSi.

We next demonstrate the evolution of the superlattice modulation with temperature in Fig. 2 and Fig. S3 (online). A similar stripe-like superlattice clearly appears at 77 K but becomes less obvious at 300 K. The enlarged FFT images corresponding to the STM topographic data at different temperatures are plotted in Fig. 2d–f, showing that the spots of superlattice are well-defined at low temperatures but fade away at 300 K. Fig. 2g shows that the peak of the spots in the FFT image broadens as the temperature raised, and the corresponding peak becomes ill-defined at the room temperature, suggesting that the period of the modulation is gradually melting (Fig. 2g). We note that the wavevector of the superlattice is temperature- and position-dependent (Fig. 2h and Fig. S4 online). To clarity it, we summarize the wavelength and the angle of the superlattice wave vectors at different temperatures from two samples in two STM systems in Fig. 2h. The wavelength and angle trend up with temperature decreasing. On Fourier space, the distribution of wavevector of superlattice also follows a certain trend with temperature.

We have noted that many defects and/or impurities introduced during sample preparation are randomly distributed on the (001) surface from the topographic data. Energy-dispersive X-ray spectroscopy measurements also show the ratio of Co and Si is not strictly 1:1 (about 0.86–0.97:1). When these defects are intensively distributed in some regions, the CDW can even be destroyed, as shown in Fig. 1e. Therefore, these defects may have an impact, but if the quantity of the defects is within a certain range, they do not affect the nature of the topology. In fact, the band structures of surface states for all materials are related to surface conditions. For topological materials, the surface state bands can be modified by surface conditions, whereas the bulk/surface correspondence will not be changed. But if the amount of the defects exceeds the tolerance of the system, the nature of the topology will be destroyed.

It is known that there are several possibilities that can induce the stripe-like superlattice modulation on a surface, such as surface reconstruction, Moiré pattern, surface strain and CDW. The possibilities of surface reconstruction, Moiré pattern and surface strain can be ruled out (see the Supplementary materials Note 1 for details). A careful analysis of spatially resolved dI/dV maps is shown in Fig. S4 (Online). Obvious contrast reversal of the stripe patterns can be observed under different biases in dI/dV mapping, which is a character of a CDW modulation. We thus conclude that the stripe-like superlattice modulation is a CDW order phase on the (001) surface, and the gap shown in STS is a CDW gap. We notice that in the weak coupling limit, the gap should be of order $2\Delta = 3.52k_BT_c$, suggesting that the observed energy gap of ~42 meV is smaller compared to that of the transition temperature of T_c > 300 K. We will discuss the reason later.

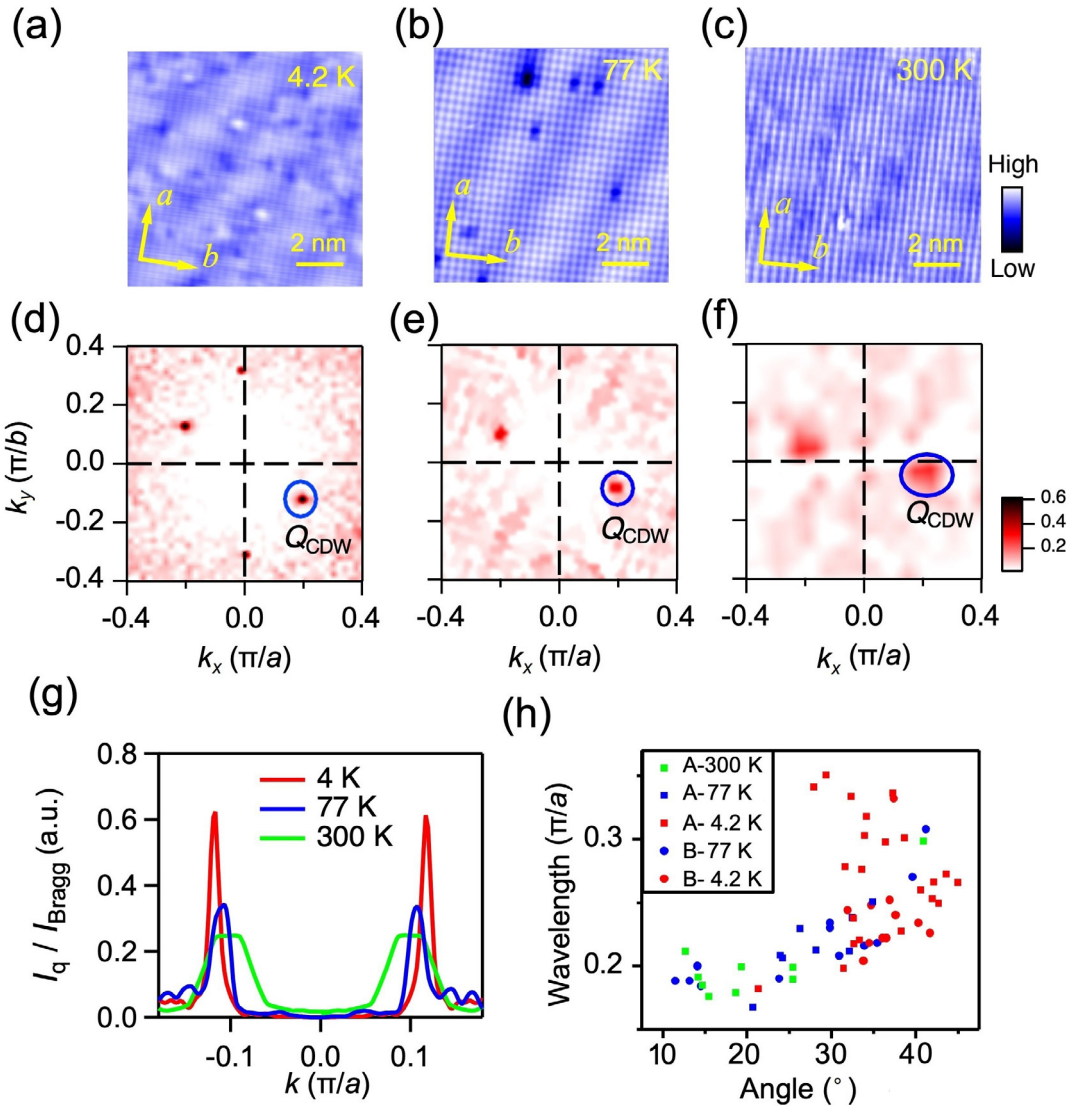

Fig. 2. (Color online) Evolution of stripe-like superlattice modulation with temperatures. (a)–(c) STM topographic image (10 nm × 10 nm) of the (001) surface of CoSi showing the stripe-like superlattice at 4.2, 77, and 300 K, respectively. (d)–(f) Zoom-in Fourier transform images of (a)–(c), with the spots corresponding to the stripe-like superlattice modulation marked by the blue circle. (g) Intensity plot along two spots of the stripe-like superlattice in (d)–(f), showing the period of superlattice slightly enlarging with temperature. (h) Relationship between the wavelength and the angle of the wave vectors at different temperatures from two samples in two STM systems (the two STM systems, A and B, are indicated in the legend).

To explore the reason why the wave vector of CDW varies with temperature, we measured the Fermi surface at different temperatures by ARPES. Fig. 3a–d show ARPES intensity maps at E_F from 50 to 200 K. The FSs at different temperatures consist of two similar Fermi arcs connecting $\bar{\Gamma}$ and $\bar{M}$. However, it is noteworthy that the Fermi arcs undergo significant deformation at different temperatures. To quantitatively describe the change of Fermi arcs, we show the momentum distribution curves (MDCs) along the yellow cut in Fig. 3d at four different temperatures (Fig. 3f). The distance between the two peaks is shown in Fig. 3e. The two Fermi arcs gradually move away from each other as the temperature decreases. Comparing MDCs at E_F of the spectrum along the cut indicated in Fig. S5c (online) at different temperatures, we found that the surface chemical potential shifts up 18 meV from 12 to 200 K. Since the Fermi arcs are formed by the helical surface states [37], the lifting of the surface chemical potential results in the two Fermi arcs approaching to each other (see the Supplementary materials Note 3 for details). So, the observed temperature-dependence of the wave vector of CDW is understandable. And the change of the two Fermi arcs at different temperatures leads to a different effective energy gap, which echoes the question of the observed smaller energy gap in our system compared with that from a simple weak coupling system.

We notice that the two long Fermi arcs near the time-reversal invariant point $\bar{X}$ are almost parallel, which is in accord with the FS nesting condition. When the Fermi arcs approach to each other with increasing temperature, the length and angle of nesting condition gradually decrease. The temperature evolution of Fermi arcs is consistent with the variation of wave vector of CDW, suggesting that the CDW is related to the Fermi arcs on the surface. We plotted the extracted $\vec{q}_{CDW}$ at 4.2 K on FS in Fig. 4c and d ($\vec{q}_{CDW}$ at 77 and 300 K on FS in Fig. S7 online). We also found that the ARPES intensity loss from high quality samples is near where their FS fits nesting condition. The good agreement between the nesting condition of two Fermi arcs and the wave vector of CDW provides a possible explanation that the CDW is induced by the partially nested Fermi arcs, which originates from the electron–electron interactions.

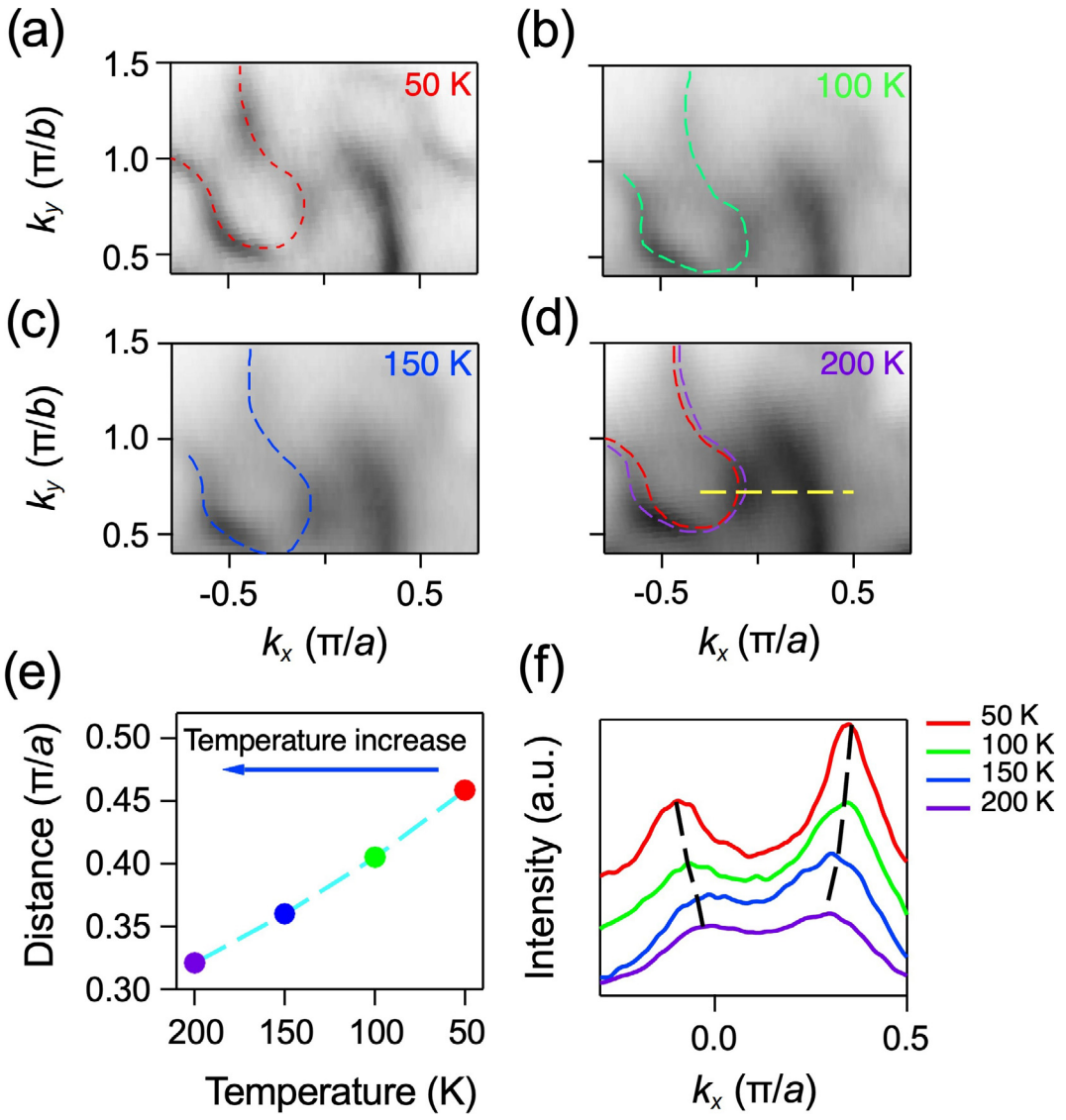

Fig. 3. (Color online) Surface chemical potential varying with temperatures. (a)–(d) ARPES intensity maps at E_F, measured with 55 eV light at (a) 50 K, (b) 100 K, (c) 150 K and (d) 200 K . The dashed lines are the guides to the eye for the Fermi arcs. (e) Relationship of the distance between two peaks shown in (f) and temperature showing the two Fermi arcs approach to each other with increasing temperature. (f) Momentum distribution curves (MDCs) along the yellow cut in Fig. 3d at four different temperatures.

In CoSi crystals, there are two kinds of enantiomers with opposite chirality in the lattices (Fig. S1a, b online), while the bulk band dispersions are exactly the same. But the signs of Chern numbers at the topological nodes are reversed because of the reversal of chiral lattice, resulting in the reversed surface Fermi arcs on the (001) surface (Fig. S1 online, details in the Supplementary materials Note 5). If the CDW is directly related to the Fermi arcs, it should be mirrored on these two enantiomers of CoSi. To verify it, we carried out measurements on the two enantiomers of CoSi. First, we performed the LEED measurements on the (001) surface of CoSi to distinguish the two enantiomers, and the mirrored Z-shaped enhanced intensity distribution manifests the opposite chirality between the two enantiomers (Fig. 4a, b). In Fig. 4c, d, the ARPES intensity maps on the two enantiomers show the mirrored configurations of the Fermi arcs, which indicates the chirality of Fermi arcs reversals (Fig. S1 online). Second, we observed mirrored stripe superlattices on the two enantiomers (Fig. 4e, f). This mirror effect can also be seen from the FFT of the topographic images (Fig. 4e, f). The mirrored CDW verifies that it is related to the nesting condition of Fermi arcs. In addition, the two enantiomers of CoSi host the same bulk FS and the same trivial pockets at the $\bar{X}$ point (Fig. 4c, d). Consequently, it furtherly indicates that the CDW is directly related to the surface Fermi arcs.

4. Conclusion

Our results provide strong evidence for the charge instability related to topological surface Fermi arcs towards a CDW phase in chiral crystal CoSi, which is the first experimental observation of many-body effect on topological boundary states. Unlike the conventional CDW phase [38–41], the wavevector of this kind of CDW is temperature-dependent. As a result, it is easy to tune the CDW phase continuously by temperature. The interaction-driven charge instability of surface Fermi arcs represents a new avenue for investigating the interplay between many-body interactions and topological boundary states. Whether other many-body responses, such as unconventional superconductivity and long-range magnetic orders, can be linked to topological boundary states remains to be further explored.

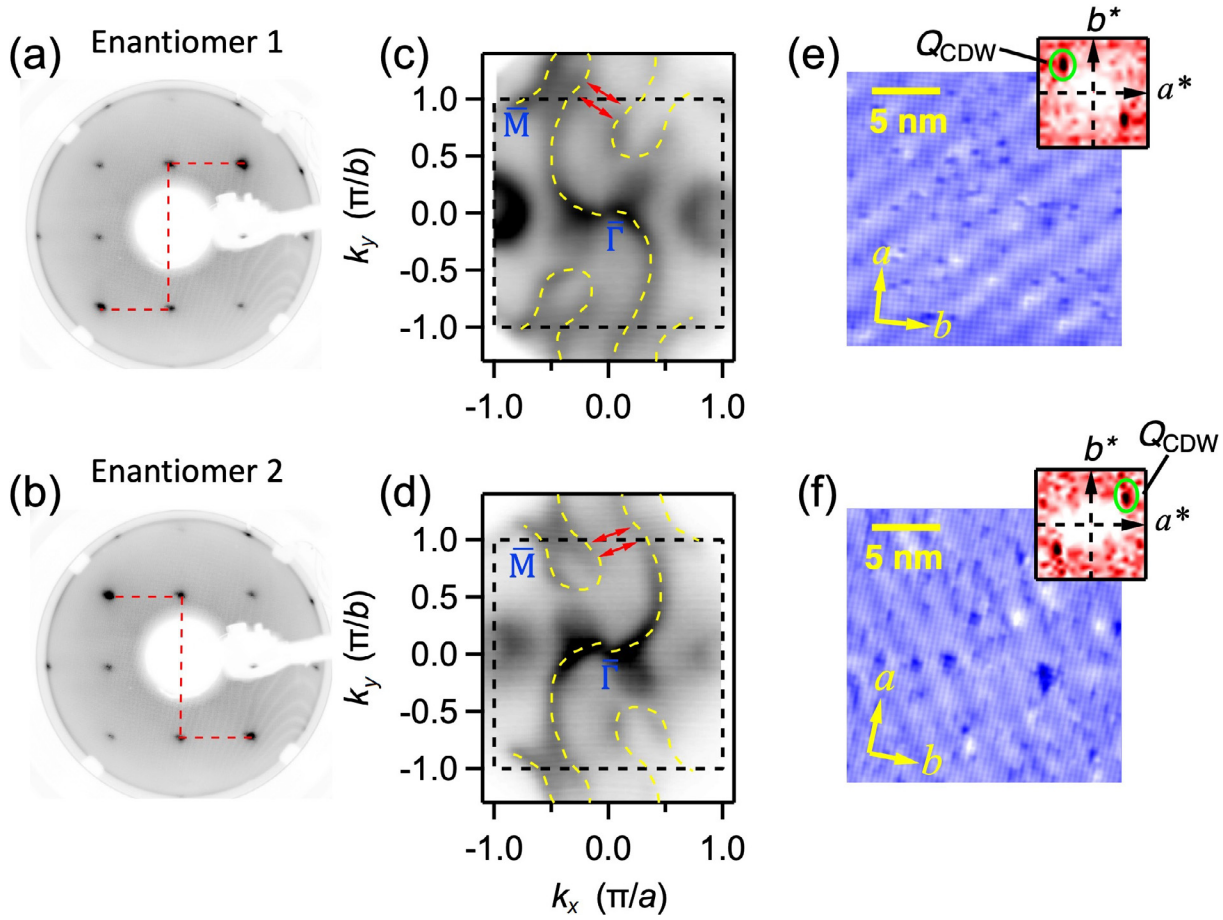

Fig. 4. (Color online) CDW phases on two enantiomers with opposite chirality. (a), (b) LEED patterns of two enantiomers with opposite chirality. The mirrored Z-shaped (the red dashed lines as the guides to the eye) enhanced intensity diffraction spots show the opposite chirality of crystal structure of two enantiomers. (c), (d) ARPES intensity maps of the two enantiomers at E_F, showing reversal chirality of Fermi arcs on the Fermi surface. The yellow dashed lines are the guides to the eye for the Fermi arcs. (e), (f) Atomically resolved STM topographic images (20 nm × 20 nm) of the two enantiomers taken at 4.2 K, showing different orientations of the CDW phases on two enantiomers. The spots (green circle) correspond to the CDW phases in the enlarged FFT images (insert), indicating that the CDW phases on the two enantiomers of CoSi are mirrored.

Conflict of interest

The authors declare that they have no conflict of interest.

Acknowledgments

We thank Lu Yu, Chen Fang, Tiantian Zhang, and Liqing Zhou for valuable discussions. We thank the technical support from Nano-X from Suzhou Institute of Nano-Tech and Nano-Bionics, Chinese Academy of Sciences (SINANO). This work was supported by the National Natural Science Foundation of China (U1832202, 11888101, 11920101005, 12141402, and 12274459), the Chinese Academy of Sciences (QYZDB-SSW-SLH043, XDB33020100, and XDB28000000), the Beijing Municipal Science and Technology Commission (Z171100002017018, and Z200005), the National Key R&D Program of China (2018YFE0202600, 2022YFA1403100, and 2022YFA1403800), the Fundamental Research Funds for the Central Universities and Research Funds of Renmin University of China (RUC) (18XNLG14, 19XNLG13, 19XNLG17, and 20XNH062), the Synergic Extreme Condition User Facility, Beijing, China, and Beijing National Laboratory for Condensed Matter Physics.

Author contributions

Zhicheng Rao, Quanxin Hu, Jinpeng Xu, and Yu-Jie Sun designed STM measurements; Quanxin Hu, Zhicheng Rao, Jinpeng Xu, and Congrun Chen performed STM measurements with assistance of Zhenyu Yuan, Renjie Zhang, Li Wang, and Fangsen Li; Zhicheng Rao performed ARPES measurements with assistance of Shunye Gao, Quanxin Hu, Jierui Huang, Wenhui Fan, and Yaobo Huang; Zhicheng Rao, Quanxin Hu, Congrun Chen, and Qing Qu processed sample surface with assistance from Jierui Huang and Cenyao Tang; Li Wang and Huaixin Yang performed TEM measurements; Shangjie Tian and Hechang Lei synthesized single crystals; Zhicheng Rao and Quanxin Hu analysed experimental data; Zhicheng Rao and Yu-Jie Sun plotted figures with assistance from Kun Jiang and Tian Qian; Zhicheng Rao, Qing Qu, Yu-Jie Sun, Kun Jiang, and Hong Ding wrote the manuscript with contributions from all authors; Yu-Jie Sun, Kedong Wang, and Hong Ding supervised the project.

Appendix A. Supplementary materials

Supplementary materials to this article can be found online at https://doi.org/10.1016/j.scib.2023.01.001.

References

[1] Kane CL, Mele EJ. Z_2 Topological order and the quantum spin hall effect. Phys Rev Lett 2005;95:146802.
[2] Fu L, Kane CL, Mele EJ. Topological insulators in three dimensions. Phys Rev Lett 2007;98:106803.

[3] Chen YL, Analytis JG, Chu J-H, et al. Experimental realization of a three-dimensional topological insulator, Bi_2Te_3. Science 2009;325:178–81.
[4] Wan X, Turner AM, Vishwanath A, et al. Topological semimetal and Fermi-arc surface states in the electronic structure of pyrochlore iridates. Phys Rev B 2011;83:205101.
[5] Weng H, Fang C, Fang Z, et al. Weyl semimetal phase in noncentrosymmetric transition-metal monophosphides. Phys Rev X 2015;5:011029.
[6] Chang C-Z, Zhang J, Feng X, et al. Experimental observation of the quantum anomalous hall effect in a magnetic topological insulator. Science 2013;340:167–70.
[7] Zhang C, Zhang Y, Yuan X, et al. Quantum hall effect based on Weyl orbits in Cd_3As_2. Nature 2019;565:331–6.
[8] Zhong S, Moore JE, Souza I. Gyrotropic magnetic effect and the magnetic moment on the fermi surface. Phys Rev Lett 2016;116:077201.
[9] Potter AC, Kimchi I, Vishwanath A. Quantum oscillations from surface Fermi arcs in Weyl and Dirac semimetals. Nat Commun 2014;5:5161.
[10] Moll PJW, Nair NL, Helm T, et al. Transport evidence for Fermi-arc-mediated chirality transfer in the Dirac semimetal Cd_3As_2. Nature 2016;535:266–70.
[11] Zhang T, Jiang Y, Song Z, et al. Catalogue of topological electronic materials. Nature 2019;566:475–9.
[12] Vergniory MG, Elcoro L, Felser C, et al. A complete catalogue of high-quality topological materials. Nature 2019;566:480–5.
[13] Tang F, Po HC, Vishwanath A, et al. Comprehensive search for topological materials using symmetry indicators. Nature 2019;566:486–9.
[14] Qi X-L, Hughes TL, Zhang S-C. Topological invariants for the fermi surface of a time-reversal-invariant superconductor. Phys Rev B 2010;81:134508.
[15] Li Y, Haldane FDM. Topological nodal cooper pairing in doped Weyl metals. Phys Rev Lett 2018;120:067003.
[16] Pesin D, Balents L. Mott physics and band topology in materials with strong spin–orbit interaction. Nat Phys 2010;6:376–81.
[17] Gooth J, Bradlyn B, Honnali S, et al. Axionic charge-density wave in the Weyl semimetal $(TaSe_4)_2I$. Nature 2019;575:315–9.
[18] Shi W, Wieder BJ, Meyerheim HL, et al. A charge-density-wave topological semimetal. Nat Phys 2021;17:381–7.
[19] Wang Z, Sun Y, Chen X-Q, et al. Dirac semimetal and topological phase transitions in A_3Bi (A=Na, K, Rb). Phys Rev B 2012;85:195320.
[20] Liu ZK, Zhou B, Zhang Y, et al. Discovery of a three-dimensional topological Dirac semimetal, Na_3Bi. Science 2014;343:864–7.
[21] Lv BQ, Feng Z-L, Xu Q-N, et al. Observation of three-component fermions in the topological semimetal molybdenum phosphide. Nature 2017;546:627–31.
[22] Ma J-Z, He J-B, Xu Y-F, et al. Three-component fermions with surface Fermi arcs in tungsten carbide. Nat Phys 2018;14:349–54.
[23] Lv BQ, Weng HM, Fu BB, et al. Experimental discovery of Weyl semimetal TaAs. Phys Rev X 2015;5:031013.
[24] Xu S-Y, Belopolski I, Alidoust N, et al. Discovery of a Weyl fermion semimetal and topological Fermi arcs. Science 2015;349:613–7.
[25] Deng K, Wan G, Deng P, et al. Experimental observation of topological Fermi arcs in type-II Weyl semimetal $MoTe_2$. Nat Phys 2016;12:1105–10.
[26] Huang L, McCormick TM, Ochi M, et al. Spectroscopic evidence for a type II Weyl semimetallic state in $MoTe_2$. Nat Mater 2016;15:1155–60.
[27] Liu DF, Liang AJ, Liu EK, et al. Magnetic Weyl semimetal phase in a Kagomé crystal. Science 2019;365:1282–5.
[28] Weng H, Liang Y, Xu Q, et al. Topological node-line semimetal in three-dimensional graphene networks. Phys Rev B 2015;92:045108.
[29] Bradlyn B, Cano J, Wang Z, et al. Beyond Dirac and Weyl fermions: unconventional quasiparticles in conventional crystals. Science 2016;353: aaf5037.
[30] Tang P, Zhou Q, Zhang S-C. Multiple types of topological fermions in transition metal silicides. Phys Rev Lett 2017;119:206402.
[31] Chang G, Xu S-Y, Wieder BJ, et al. Unconventional chiral fermions and large topological Fermi Arcs in RhSi. Phys Rev Lett 2017;119:206401.
[32] Rao Z, Li H, Zhang T, et al. Observation of unconventional chiral fermions with long Fermi arcs in CoSi. Nature 2019;567:496–9.
[33] Sanchez DS, Belopolski I, Cochran TA, et al. Topological chiral crystals with helicoid-arc quantum states. Nature 2019;567:500–5.
[34] Takane D, Wang Z, Souma S, et al. Observation of chiral fermions with a large topological charge and associated Fermi-arc surface states in CoSi. Phys Rev Lett 2019;122:076402.
[35] Schröter NBM, Stolz S, Manna K, et al. Observation and control of maximal Chern numbers in a chiral topological semimetal. Science 2020;369:179–83.
[36] Tang C-Y, Rao Z-C, Yuan Q-Q, et al. Atomically flat surface preparation for surface-sensitive technologies. Chin Phys B 2020;29:028101.
[37] Fang C, Lu L, Liu J, et al. Topological semimetals with helicoid surface states. Nat Phys 2016;12:936–41.
[38] Gao S, Flicker F, Sankar R, et al. Atomic-scale strain manipulation of a charge density wave. Proc Natl Acad Sci USA 2018;115:6986–90.
[39] Wilson JA, Di Salvo FJ, Mahajan S. Charge-density waves and superlattices in the metallic layered transition metal dichalcogenides. Adv Phys 1975;24:117–201.
[40] Rice TM, Scott GK. New mechanism for a Charge-Density-Wave instability. Phys Rev Lett 1975;35:120–3.
[41] Makogon D, van Gelderen R, Roldán R, et al. Spin-density-wave instability in graphene doped near the van Hove singularity. Phys Rev B 2011;84:125404.

Zhicheng Rao received his Ph.D. degree from Institute of Physics, Chinese Academy of Sciences (IOP, CAS) in 2022. His current research interest mainly focuses on the properties of topological boundary states on correlated system by angle resolved photoemission spectroscopy and scanning tunnelling microscopy.

Quanxin Hu received his B.S. degree from University of Chinese Academy of Sciences in 2018. He is currently a Ph.D. candidate at IOP, CAS. His research interest is the topological and superconducting properties of correlated materials.

Shangjie Tian received his Ph.D. degree in 2022 from Renmin University of China. He is currently a postdoctoral of Anhui University. His research interest lies in the topological or magnetic materials, from crystal growth and characterization of physical properties to understanding the underlying physics mechanism.

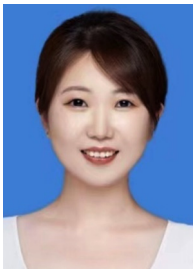

Qing Qu is currently a postdoctoral researcher at Department of Physics, Southern University of Science and Technology. She obtained her Ph.D. degree from The Hong Kong University of Science and Technology (HKUST) in 2021, and then worked at HKUST as a postdoctoral researcher. Her current research interest mainly focuses on molecular beam epitaxy and exploration of unconventional superconductivity and strongly correlated electronic systems using scanning tunnelling microscopy.

Jinpeng Xu is currently an associate professor at IOP, CAS. Before joining IOP, he spent 4 years on working at the University of Hong Kong and City University of Hong Kong as a postdoctoral researcher. He obtained his Ph.D. degree in Physics from Shanghai Jiao Tong University in 2015. His research focuses on synthesis of materials using molecular beam epitaxy, and *in-situ* investigation of Majorana bound states, unconventional superconductivity, strongly correlated effects and topological orders by scanning tunnelling microscopy.

Hechang Lei is currently a professor at Department of Physics, Renmin University of China. He received his Ph.D. degree from Institute of Solid State Physics, CAS in 2009. His current research interest mainly focuses on exploration of novel strongly correlated electronic systems, topological materials and low-dimensional materials as well as understanding exotic physical phenomena in these systems.

Yu-Jie Sun obtained his B.S. and Ph.D. degrees (2009) from the Tsinghua University. He worked at IOP, CAS before joining Southern University of Science and Technology in 2021. His research interest focuses on high-temperature superconductors, interface superconductors and topological materials.